

Spatially resolved mass flux measurements with dual comb spectroscopy

David Yun^{1,*}, Ryan K. Cole¹, Nathan A. Malarich¹, Sean C. Coburn¹, Nazanin Hoghooghi¹, Jiwen Liu², Jacob J. France³, Mark A. Hagenmaier⁴, Kristin M. Rice⁴, Jeffrey M. Donbar⁴, Gregory B. Rieker^{1,5}

¹*Precision Laser Diagnostics Laboratory, Department of Mechanical Engineering, University of Colorado Boulder, Boulder, CO 80309, USA*

²*Taitech Scientific Solutions Incorporated, Beavercreek, OH 45430*

³*Innovative Scientific Solutions Incorporated, Dayton, OH 45459*

⁴*U.S. Air Force Research Laboratory, Wright-Patterson AFB, OH, 45433, USA*

⁵*email: greg.rieker@colorado.edu*

**Corresponding author: david.yun@colorado.edu*

Abstract: Providing an accurate, representative sample of mass flux across large open areas for atmospheric studies or the extreme conditions of a hypersonic engine is challenging for traditional intrusive or point-based sensors. Here, we demonstrate that laser absorption spectroscopy with frequency combs can simultaneously measure all of the components of mass flux (velocity, temperature, pressure, and species concentration) with low uncertainty, spatial resolution corresponding to the span of the laser line of sight, and no supplemental sensor readings. The low uncertainty is provided by the broad spectral bandwidth, high resolution, and extremely well-known and controlled frequency axis of stabilized, mode-locked frequency combs. We demonstrate these capabilities in the isolator of a ground-test supersonic propulsion engine at Wright-Patterson Air Force Base. The mass flux measurements are consistent within 3.6% of the facility-level engine air supply values. A vertical scan of the laser beams in the isolator measures the spatially resolved mass flux, which is compared with computational fluid dynamics simulations. A rigorous uncertainty analysis demonstrates a DCS instrument uncertainty of ~0.4%, and total uncertainty (including non-instrument sources) of ~7% for mass flux measurements. These measurements demonstrate DCS as a low-uncertainty mass flux sensor for a variety of applications.

© 2022 Optica Publishing Group under the terms of the [Optica Publishing Group Open Access Publishing Agreement](#)

1. Introduction

Accurate measurements of gaseous mass flux, the total flow rate of molecules through a volume, are essential to many research fields. For example, species mass flux measurements have been used to study greenhouse gas emissions of cities and arctic environments [1–6], evapotranspiration of forests and agricultural sites [7–9], and atmospheric effects of wildfires [10,11]. Mass flux measurements are also useful for a host of engineering applications, such as aeropropulsion research, where air mass flux is essential for analyzing inlet phenomena in hypersonic engines [12], determining flow enthalpies in arc-jet facilities [13], and characterizing impulse in rotating detonation engines [14]. However, direct measurements are extremely challenging in large-scale open environments and environments with extreme flow phenomena because it is difficult to measure all of the components of mass flux (velocity and density, the latter being derived from temperature, pressure, and mixture composition). Here, we demonstrate non-intrusive, absolute measurements of mass flux in such environments with low uncertainty by leveraging the unique properties of stabilized, mode-locked frequency combs. In particular, the extremely precise and well-known spacing between the optical ‘teeth’

of the comb creates a near-perfect ruler against which to measure the velocity-dependent Doppler shift and the pressure-dependent widths of molecular absorption features. The broad optical bandwidth of the combs enables measurement of a multitude of absorption features whose relative intensity collectively define the temperature of the gas. The optical bandwidth also enables accurate measurement of the gas composition, including the potential to resolve multiple gas species at once.

We use frequency combs to measure the mass flux in a direct-connect, ground-test, dual-mode ramjet propulsion system at the Air Force Research Laboratory. Scramjets/ramjets are air-breathing engines which typically operate at speeds above Mach 5. While short duration scramjet flights have been demonstrated via programs such as X-51 [15] and HIFiRE Flight 2 [16], achieving consistent operation requires improved understanding and optimization of engine designs. Specifically, complex flow patterns due to shock-boundary interactions around the supersonic inlet of flight vehicles (see Figure 1a) can lead to uncertainty in the inlet air mass flux. This in turn requires overdesign of flight surfaces and inlet properties to accommodate these uncertainties, at the expense of flight performance.

We determine the air mass flux with low uncertainty by measuring velocity, temperature, pressure, and species mole fraction through absorption spectroscopy of hundreds of water vapor quantum transitions in the $6880 - 7186 \text{ cm}^{-1}$ spectral region (1392 – 1453 nm) with $\sim 46,000$ optical frequencies (comb teeth) of a stabilized all-fiber mode-locked dual frequency comb spectrometer. We take several measurements at varying flow conditions at the centerline of the dual-mode ramjet. This choice of facility allows for comparisons to both computational fluid dynamics (CFD) calculations and upstream facility flow rate measurements which are expected to have high accuracy as the facility is a closed, direct-connect system. Additionally, we perform a vertical scan at a single flow condition to within 1 mm from the wall to provide a mass flux spatial profile. The measured flow properties and resulting air mass flux results are compared to facility measurements and computational fluid dynamics (CFD) calculations across a range of flow conditions. Through a detailed analysis, we estimate 0.4% instrument uncertainty in the measured mass flux. Additional systematic uncertainties bring the overall uncertainty to $\sim 7\%$, largely due to uncertainty in the absorption model that is used to interpret the instrument measurements (and which can be improved in the future).

This is the first demonstration of dual comb absorption spectroscopy (DCS) measurements of air mass flux, and the first demonstration of DCS in a hypersonic aeropropulsion environment. Our results demonstrate the potential of broadband dual-comb spectroscopy for accurate, precise, and nonintrusive mass flux measurements in high-speed flows. While the DCS system used here is based on H_2O absorption in the near-infrared spectral region, the mode-locked frequency comb spectral range can be tailored to encompass measurements of more species relevant to greenhouse gas monitoring and combustion [17–23]. Additionally, works such as [24–28] have demonstrated that DCS instrument measurements can be easily expanded to large areas and open environments, enabling mass flux measurements for large-scale studies in environmental, atmospheric, and agricultural research. Recent work on chip-sized frequency combs [29–31] and electro-optic frequency combs will further open mass flux measurement possibilities for DCS [32–34].

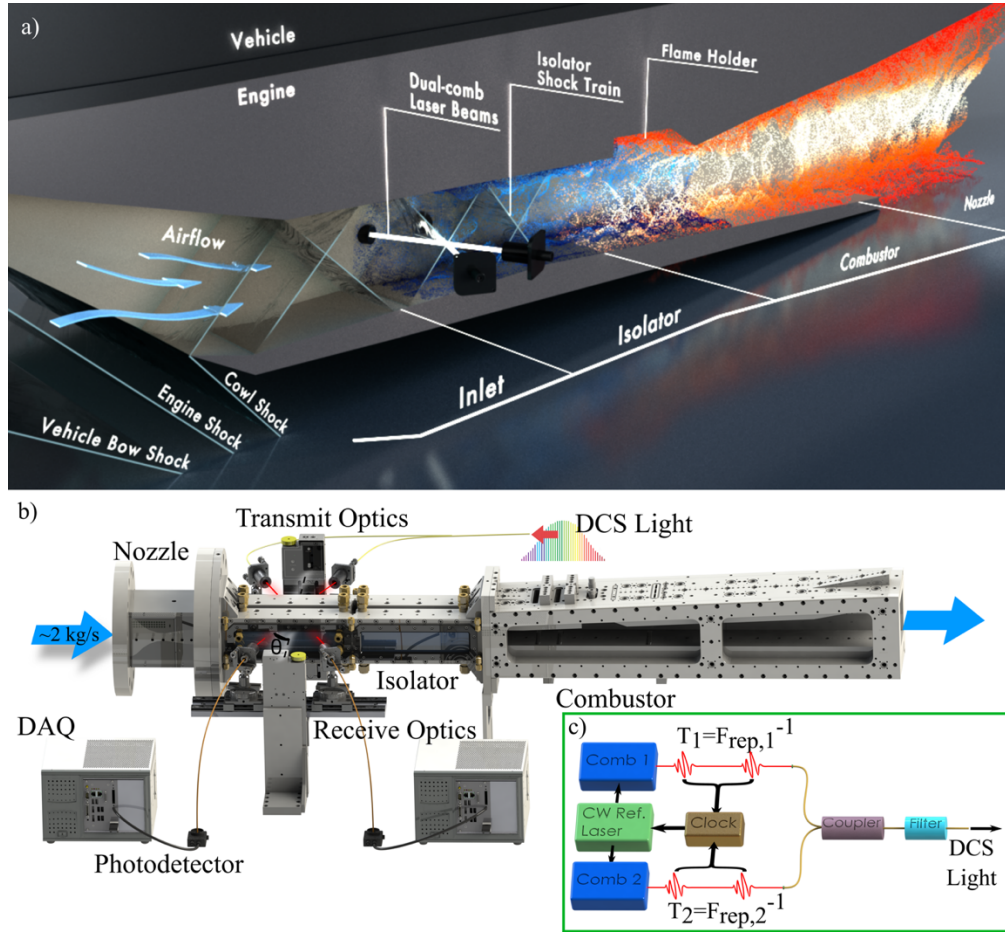


Fig. 1. DCS measurements in a dual-mode ramjet test engine. (a) The main components of a ramjet/scramjet are the inlet and isolator which compress the air via an oblique shock train, the combustor which injects and ignites fuel to heat the air, and a nozzle which expands and accelerates the air creating thrust. (b) Light from the frequency combs launch into the isolator at angle θ . Resulting light is caught onto multi-mode fiber and detected on a pair of fast photodetectors via a high-speed FPGA data acquisition system. Pitch and catch optics are placed on translation stages to allow for measurements at different heights. (c) DCS consist of two frequency combs whose repetition rates are read by a highly accurate clock and tightly controlled by a reference laser. Light from both combs is combined via a coupler and filtered to the H_2O infrared absorption band.

2. Dual frequency comb spectroscopy for air mass flux measurements

2.1 Optical mass flux measurement

Mass flux is the product of the velocity (U) and density (ρ) in a flow.

$$\dot{m} = \rho U \quad (1)$$

If we assume that the composition of the gas besides H_2O (the molecular absorption target for the present measurement) is dry air, we can determine the density via the ideal gas law using temperature, pressure, and H_2O concentration and ultimately calculate mass flux with the following equation:

$$\dot{m} = \frac{(\chi_{H_2O}M_{H_2O} + (1 - \chi_{H_2O})M_{air})PU}{RT} \quad (2)$$

Here M_{H_2O} and M_{air} are the molar masses of water and dry-air, and R is the gas constant. The rest of the terms: pressure (P), temperature (T), H_2O concentration (χ_{H_2O}), and velocity (U), can be extracted from laser absorption spectra measured with an appropriate optical configuration and laser.

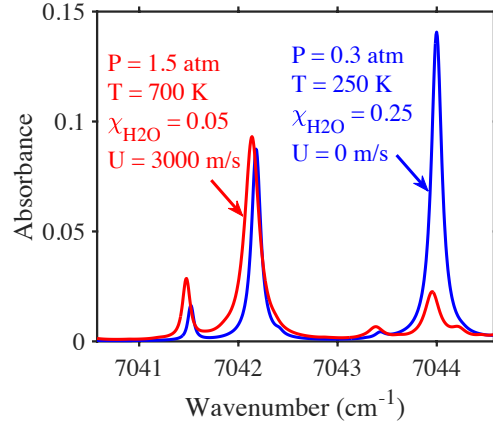


Fig. 2. H_2O absorption features at two different thermodynamic conditions: $P = 0.3 \text{ atm}$, $T = 250 \text{ K}$, $\chi_{H_2O} = 0.25$, $U = 0 \text{ m/s}$ (blue) and $P = 1.5 \text{ atm}$, $T = 700 \text{ K}$, $\chi_{H_2O} = 0.05$, $U = 3000 \text{ m/s}$. Here, the Doppler shift is associated with a beam angle of 35° to the normal of the flow direction.

DCS (and laser absorption spectroscopy in general) measures laser absorption at frequencies resonant with the rovibrational quantum state transitions of a constituent molecule in a gas sample or flow. Figure 2 shows a small portion of the H_2O absorption spectrum to demonstrate the large differences in the spectrum that are induced by different velocity, pressure, temperature, and species concentration. Flow velocity induces a Doppler shift in the absorption feature positions if the laser beam is angled upstream or downstream to the bulk gas flow [35]. In the present measurement, we configure the two beams in a crossed configuration with one beam angled upstream and the other downstream with equal angles (see Fig. 1a). In this case, equal and opposite Doppler shifts are induced in the absorption spectra measured with each beam. The width of the absorption features is proportional to pressure. The magnitude of the absorption features is proportional to the species concentration. Finally, the relative intensities between the features in the spectrum are dependent on temperature, because absorption transitions arise from quantum states with different lower state energies. Thus, pressure, species concentration, velocity, and temperature of the probed region of the flow can be determined by comparing the size, shape, and position of measured absorption features with an absorption model of the expected spectra for a given set of conditions.

2.2 Dual frequency comb spectroscopy

Mode-locked frequency comb lasers have emerged as powerful sources for absorption spectroscopy [36,37], which can be used to simultaneously measure all of the components of mass flux. Frequency combs emit a train of optical pulses comprising multitudes of evenly spaced, discrete optical frequencies (referred to as “comb teeth”) across a broad spectral bandwidth. The optical frequencies of the comb teeth are related through Eq. 3:

$$f_n = nf_{rep} + f_0 \quad (3)$$

where f_0 is the carrier envelope offset frequency, n is the comb tooth number, and f_{rep} is the pulse repetition rate of the laser. Thus, the absolute frequency of each individual comb tooth is set with only two degrees of freedom (f_{rep} and f_0). These parameters can be precisely measured and controlled (as described below) to create a near-perfect optical ruler with which to measure the position, shape, and magnitude of absorption features.

A key challenge in spectroscopy with frequency combs is reading out the absorption information contained in the thousands of individual optical frequencies after they have traveled through the environment of interest. We address this challenge using dual comb spectroscopy (DCS), in which two frequency combs are coherently locked to one another with slightly different comb tooth spacing. The combs are interfered on a photodetector to down-convert pairs of comb teeth from their optical frequencies to corresponding heterodyne beat signals at easily detectable radio frequencies [38]. The attenuation of the comb teeth by absorption is reflected in the strength of the heterodyne beat signals, and thus the absorption spectrum can be read out on a tooth-by-tooth basis maintaining the frequency accuracy and precision of the combs themselves. The detection requires a single fast photodetector to capture the interference signal (the interferogram), which yields the laser transmission spectrum after applying a Fourier transform.

The frequency combs used here are Erbium-doped, polarization-maintaining-fiber based frequency combs with a pulse repetition rate of 200 MHz [39]. Figure 1c shows an overview of the DCS configuration. The f_0 of each frequency comb is stabilized using the f -to- $2f$ locking scheme [40,41]. In this approach, each comb is broadened across an octave of optical frequency space, and a tooth from one end of the spectrum is frequency doubled and interfered with a tooth from the other end of the spectrum. The heterodyne beat frequency between the two teeth is exactly f_0 , which we stabilize at a specific RF frequency through feedback to the frequency comb oscillator pump current. Additionally, a tooth from each frequency comb is phase-locked to a common 2 kHz linewidth continuous wave (CW) reference laser. This establishes mutual coherence between the two comb sources, and provides the means to stabilize the second degree of freedom (f_{rep}) of each comb. Specifically, the heterodyne beat frequency between the CW laser and the tooth from each laser is measured with a frequency counter and stabilized through feedback to high-speed piezoelectric transducers glued to the fibers of each laser cavity. The repetition rate for each laser is also continuously measured using a frequency counter, and we use slow feedback to the CW laser current (which controls the CW laser wavelength) to maintain stable f_{rep} [42].

Using this stabilization approach, the quality of the optical ruler for measuring the absorption spectrum is set by the stability and accuracy of the frequency reference for the frequency counters, and the amount of drift in f_{rep} allowed by the CW laser feedback. In this study the frequency reference is a simple ovenized quartz oscillator (Wenzel 501-27514-21) with a relative frequency accuracy of 1.5 ppm. The CW laser digital feedback loop allows a drift in f_{rep} of less than 25 ppb. Thus, the frequency reference is the limiting factor in the ultimate accuracy of the comb tooth frequencies. Still, the 1.5 ppm relative accuracy of the frequency reference enables the spacing of the comb teeth to be known to within ~ 300 Hz (1.0×10^{-8} cm $^{-1}$) at all times and the absolute position of teeth to within 300 MHz (0.011 cm $^{-1}$). This leads to low instrument uncertainty, as described later. If further accuracy is required the frequency reference can be replaced with a GPS-disciplined oscillator which has a relative accuracy of 10 ppt, and the feedback to the CW laser can be improved by switching to a high-speed analog control feedback on the CW laser to stabilize f_{rep} .

With the dual-comb spectrometer employed in this study, we achieve ~ 300 cm $^{-1}$ optical bandwidth encompassing hundreds of H $_2$ O absorption features with a spectral point spacing of 0.0067 cm $^{-1}$. Each spectrum is acquired in 0.7 ms (though many are averaged to reach high SNR). These mode-locked dual frequency comb spectroscopy performance metrics thus blend the bandwidth of Fourier Transform Infrared Spectrometry (FTIR) with the resolution and

acquisition speed of tunable diode laser absorption spectroscopy (TDLAS), with frequency referencing that far exceeds both FTIR and TDLAS. For example, a TDLAS measurement with a 15 cm etalon reference would need real-time knowledge and control of the etalon length to 225 nm to achieve the frequency referencing performance of the dual comb.

2.3 Instrument uncertainty

The DCS performance characteristics relate directly to low *instrument* uncertainty for each of the measured components of mass flux. We define *instrument* uncertainty to be the fundamental limit of the measurement uncertainty imparted by the stability and accuracy of the DCS. For velocity measurements, the absolute frequency error of the frequency combs cancel in the crossed beam configuration (see Supplement 1), and only uncertainty in the comb teeth spacing imparts an instrument uncertainty. As stated above, this is controlled to 0.00015%, and sets the lower limit of achievable uncertainty in the measurement of velocity. The uncertainty of the comb tooth spacing also defines the lower limit of the achievable instrument uncertainty for pressure measurements (which are based on the relative width of the measured absorption features). We found that for pressure, temperature, and species concentration retrievals, uncertainty in the frequency axis also leads to additional error during the fit of the absorption model to the measurement due to correlation between the parameters (since all are retrieved simultaneously). As described in Supplement 1 these uncertainties are still very low; 0.012% for pressure, 0.015% for species concentration, and 0.0042% for temperature.

While difficult to quantify, the DCS bandwidth, resolution, and lack of instrument lineshape (distortion) also help reduce uncertainty in the measurement [43]. By incorporating many features, scatter in the absorption model error from feature to feature are averaged out. Additionally, the broad bandwidth increases robustness against optical interference effects such as etalons and ambiguities in laser intensity baseline which can distort feature intensity retrievals [44]. For temperature, incorporating a multitude of features from different lower state energies offers improved dynamic range and reduced uncertainty with respect to traditional tunable laser two-line thermometry [45].

Altogether, mode-locked DCS is therefore well-suited for mass flux measurements due to the low levels of uncertainty that are achievable through the quality of the optical spectrum reference, its broad bandwidth and high resolution, and point spacing accuracy. We describe later that background absorption, noise, absorption model error, laser angle uncertainty, and other systematic uncertainties outside of the DCS instrument itself increase the overall uncertainty. However, many of these systematic uncertainties can continue to be improved through changes to the optical setup and better absorption models.

3. DCS experiment in a direct-connect dual-mode ramjet engine

We demonstrate dual comb mass flux sensing in a continuous-flow, direct-connect, supersonic combustion research facility at Wright-Patterson Air Force Base [46]. The test article is a ground-test dual-mode ramjet. A dual-mode ramjet can operate in either ramjet or scramjet mode. Ramjets and scramjets are air-breathing engines which typically operate at speeds above Mach 5 and slow and compress air with a series of shock waves as opposed to the fans and turbomachinery common to lower-speed engines. Scramjets differ from ramjets in that air in the engine never slows below the speed of sound allowing for faster flight speeds. Figure 1a shows a schematic of a dual-mode ramjet. During supersonic flight, air passes through shockwaves emanating from the leading edges of the aircraft. It then enters the inlet/isolator region and is further compressed by a series of shock waves that raises the pressure and temperature of the air, while reducing its velocity. Fuel is then mixed with the air and ignited in the combustor. The flow finally expands through a nozzle to provide thrust. Air mass flux through the engine is a critical parameter. Taken together with fuel flow rate and thrust, the

overall performance of the engine can be assessed. It is a difficult parameter to measure, as intrusive diagnostics cause performance-changing perturbations in supersonic environments. It is also a difficult parameter to calculate for ‘free-jet’ ground-test facilities (where the test article is placed inside a supersonic wind tunnel), or flight engines, where there is high uncertainty regarding the air flow into versus around the engine.

The isolator of a direct-connect test facility is ideal for this initial demonstration because the mass flux can be determined with reasonable accuracy based on the test facility air flow measurements (all of the air flow from the facility compressors are directed through the test article in a direct-connect facility). The test article is 10.2 cm wide, 3.8 cm tall, and 61 cm long with optical access via 2.1-cm-thick quartz windows. See Supplement 1 for a more detailed description of the dual-mode ramjet test model.

We place the dual-comb spectrometer in a control room adjacent to the test cell. A coupler combines light from each of the two combs and splits the combined light onto two single-mode fibers. The light passes through free-space optical filters and back into single-mode fiber for transmission to the test cell. In the test cell, the light is collimated and passed through the isolator windows. We set both optical paths parallel to the bottom of the isolator. Using high precision rotation mounts we angle one beam in an upstream-propagating direction and the other in a downstream-propagating direction (hereafter referred to as the upstream and downstream beam respectively) at angles of 35° and -35° respectively from the normal of the isolator windows, as shown in Figure 1b. After passing through the isolator, the light is focused into multimode optical fibers via 1 cm diameter optics that are robust to the intense turbulence-induced beam steering that occurs through the test section. The transmit and receive optics rest on vertical translation stages that enable measurements at different heights in the isolator. The DCS signals are measured by photodetectors and recorded on two separate 250 MS/s digitizers, which are both clocked by the pulse repetition rate of one of the combs.

We obtain spectra between $6880 - 7186 \text{ cm}^{-1}$ ($1392 - 1453 \text{ nm}$) using 46,000 comb teeth (each with $\sim 25 \text{ kHz}$ linewidth) at a rate of 1.4 kHz (Figure 3). This region spans hundreds of observable H_2O absorption features. The spectra are phase-corrected and averaged for 60 seconds. Figure 3a shows the transmission spectra from the highest velocity condition (run 5). We fit the measured spectra using the modified free induction decay approach [44], which enables baseline-free fitting and rapid computations. The fits use absorption models created from the high-temperature H_2O absorption database developed by Schroeder et al. [47], which improves upon HITRAN2012 [48] especially for the high-temperature conditions present in the isolator. An example model generated at the best-fit conditions is compared with the data in Figure 3d. All open-air optical paths outside of the test engine are purged with dry air to reduce interfering background absorption from ambient water vapor. Remaining background absorption is measured before and after each ramjet run with cold dry air flowing through the isolator and subtracted from the operational run data as described in Supplement 1.

The mass flux measurement is localized to the vertical and axial (streamwise) location of the crossed lasers. This results in a 7 cm streamwise spatial resolution due to the angling of the lasers and a 1 mm height resolution corresponding to the beam diameter. In this study, we demonstrate spatially resolved measurements in the vertical direction by scanning the crossed beams vertically. The flow conditions tested here were designed to be simple (i.e. no distortion generator or isolator shock train), so that the DCS measurements could be readily compared with area-normalized facility mass flow rate measurements and CFD calculations. This resulted in minimal gradients along the axial direction of the isolator. Future measurements of more complex conditions could include translation of the laser beams in the axial direction to achieve a 2D measurement of the flowfield.

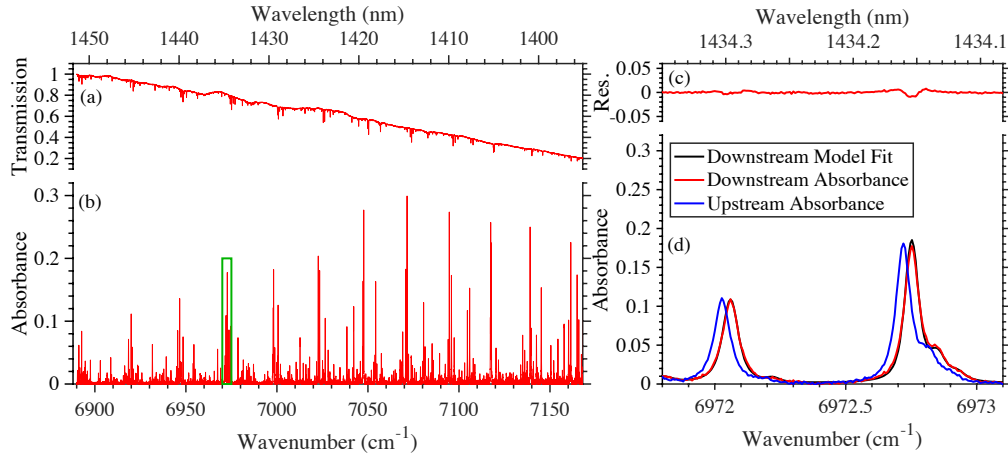


Fig. 3. Measured spectra from run 5 with 60-second averaging. Panel a) shows the transmission spectrum from the downstream-propagating beam. Panel b) shows the corresponding absorbance spectra with laser intensity baseline and background absorbance removed. Panel d) shows a zoom view of the absorbance spectrum corresponding to the green box in panel b) together with the fitted model and the upstream-propagating beam spectrum. Panel c) shows the fitted residual (data-model) for the downstream-propagating spectra.

4. Results and CFD comparison

4.1. Centerline measurements

In the first test configuration, we perform measurements at the centerline of the isolator (19 mm from the bottom) while the facility parameters are varied to produce different velocity, temperature, and pressure conditions (tabulated in Supplement 1). The DCS measurement results for velocity, temperature, pressure, χ_{H_2O} , and the consequent total mass flux calculations are shown in Figure 4.

The simple flow conditions in this study feature a uniform core flow with relatively small boundary layers. Thus, a centerline measurement can be reasonably compared against area-normalized facility mass flow rate measurements. We chose a direct-connect facility (where the entire mass flow of the facility compressors must pass through the engine) so that the compressor mass flux could serve as a direct comparison with the measurements. The facility mass flow rate measurements are taken with flow meters upstream of the isolator which are expected to have low uncertainties. We normalize the flow rate with the isolator cross-sectional area to provide a facility-derived mass flux, which is shown in Figure 4. The measurements are within 0.1% to 3.6% of the facility-derived mass flux across all tests. As discussed later, we estimate the DCS mass flux uncertainty to be 7%. The mass flux measurements thus agree within their uncertainty to the facility values, suggesting that the uncertainty estimate is correct (if not conservative).

The facility measurements only enable mass flux comparisons, so we use a 3D CFD flow solution for comparison with the other measured parameters (velocity, temperature, species concentration and pressure). The simulations are performed in CFD++ (Metacomp Technologies, Inc.) based on a full 3D Reynolds-Averaged Navier Stokes approach with the two-equation cubic $k - \epsilon$ turbulence model and an isothermal wall condition. To compare the CFD and DCS values, we simulate a line-of-sight absorption measurement through the CFD at the same location as the real-world measurement [49]. We extract flow properties voxel-by-voxel along a simulated beam path through the CFD to produce an integrated absorption that accounts for nonuniformities in flow parameters. CFD-derived flow values are then extracted from the simulated integrated spectra using the same fitting algorithm used to fit the DCS spectra. This process minimizes any differences between DCS and CFD values due to

nonuniformity in the flow. The CFD-derived values for all of the measured parameters are shown in Figure 4. The CFD-derived parameters track the DCS-measured parameters. The CFD-derived velocities are within 2.6% of the DCS measured values. The CFD-derived temperature differs most from the DCS temperature at run 5 (4.8%) while differing less than 4% for other runs. The CFD-derived χ_{H_2O} and pressure values exhibit the largest deviations from the DCS measured values, up to 6.1% and 7.3%, respectively. These differences result in a total difference between the CFD-derived and DCS-measured mass flux ranging between 3.1% and 8.8%. We note that the CFD-derived values fall farther from the facility-measured mass flux than the DCS measurements for all conditions. We show in the next section that spatially resolved measurements are helpful in assessing how different CFD boundary conditions influence the ultimate CFD result, and can help improve the CFD results.

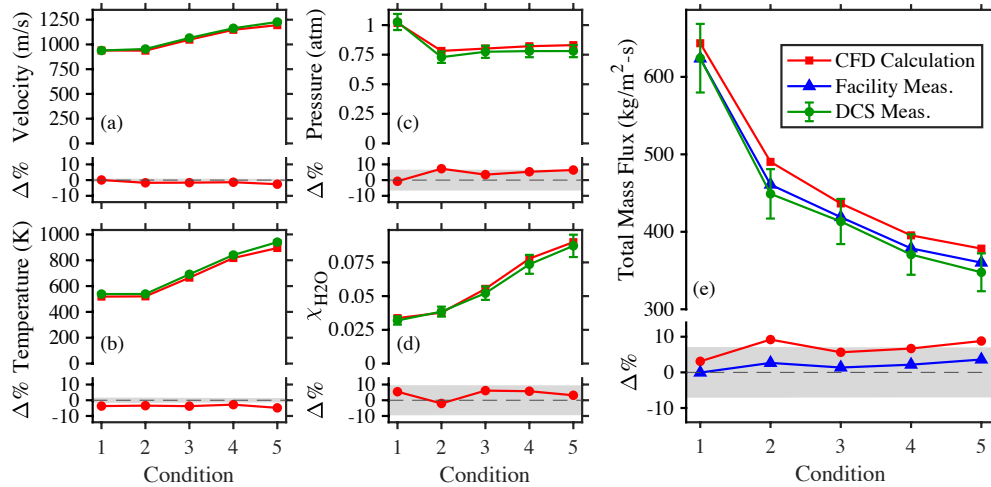


Fig. 4. DCS measurements with uncertainties at the centerline of the isolator for different flow conditions. The DCS fit results (green circles) of velocity (a), pressure (b), temperature (c), χ_{H_2O} (d), and total mass flux (e) are compared to CFD (red squares) with isothermal wall boundary conditions. Each panel has a corresponding residual plot that shows the difference between DCS and CFD values, defined as $(CFD-DCS)/DCS$, with a shaded gray area denoting the DCS measurement uncertainty. Panel e) also shows a comparison to the facility-derived mass flux values (blue crosses).

4.2. Vertical scan

In the second measurement configuration, we scan the crossed beams vertically from the centerline to within 1 mm of the bottom wall while the isolator flow is maintained at one condition. Figure 5 shows the measurement configuration. The measurements span 7 cm in the axial (streamwise) direction as the beams traverse the isolator at $\theta = 35^\circ, -35^\circ$. The span along the vertical axis is limited to the beam width, which is ~ 1 mm. Thus the axial resolution is 7 cm and the vertical resolution is 1 mm. Narrower laser beam angles would improve the axial resolution at the expense of velocimetry precision (not accuracy). Figure 5 also shows the CFD-predicted mass flux in the measurement region. One can see that the flow is mostly uniform in the axial direction and that the largest gradient occurs in the vertical direction near the wall. Therefore, we take measurements at 19 mm (centerline) and 9 mm to represent the core flow, and measurements at 3 mm, 2 mm, and 1 mm to profile the boundary layer near the floor (cowl) of the isolator.

Figure 6 shows the DCS vertical profile measurements of the different parameters and the mass flux. The measurements agree with expectations for the various parameters. Velocity is uniform in the core of the flow and decreases at the boundary layer, which is approximately 3-5 mm thick at the bottom of the isolator at this location. Temperature increases near the wall,

as expected for supersonic flows where slowing of the gas near the walls increases the static temperature of the gases. Pressure is relatively uniform across the isolator, which we expect for the simple flow conditions used for these experiments (no distortion generator to produce a pronounced oblique shock train in this region of the isolator). Remaining subtle variations in pressure could be due to weak shock disturbances in the flow. Finally, χ_{H_2O} is relatively stable across the isolator, which is expected since water vapor is neither produced nor destroyed in the isolator or near the boundaries.

Figure 6 also incorporates the CFD-derived values of the various parameters. For these experiments, we provide two CFD calculations – one assuming an adiabatic boundary condition at the walls and one assuming an isothermal boundary condition at the walls. The difference between the CFD calculations is primarily visible at the boundary layer. All parameters from both CFD simulations are within 14% of the DCS-measured values. In general, the CFD simulation with adiabatic boundary conditions tends to agree better than the isothermal condition in the boundary layer. Similarly, the adiabatic air mass flux values have better agreement than the isothermal values in the boundary layer. Thus spatially resolved DCS data can provide an important benchmark and means for tuning CFD in hypersonic flows.

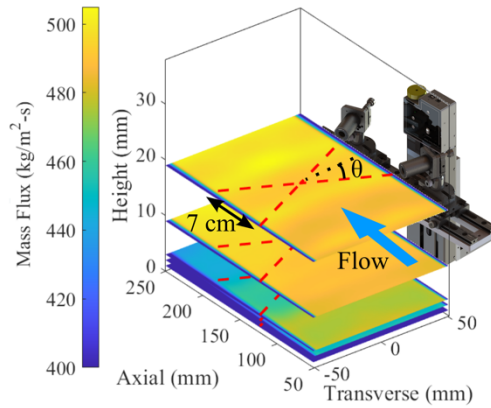


Fig. 5. DCS measurement configuration for the vertical scan experiments. Measurements are taken at different heights across the isolator at constant flow condition by moving optics with a translation stage. Slices of the CFD-predicted mass flux are included at each height to show the expected gradients in the measurement region.

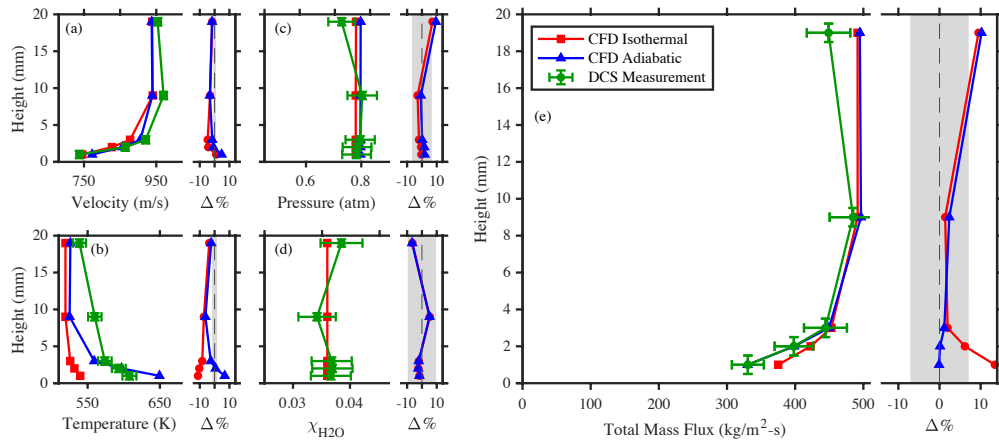


Fig. 6. DCS fit results (green circle) of velocity (a), pressure (b), temperature (c), and χ_{H_2O} (d) and calculated total mass flux (e) compared to CFD for the vertical scan of the lower half of the isolator. Here, both CFD assuming isothermal boundary condition (red circle) is shown alongside CFD assuming adiabatic boundary condition (blue triangle). Differences between DCS and CFD, which is defined as (CFD-DCS)/DCS, is shown to the right of each of the DCS-CFD comparison plots with a grey shaded area indicating the DCS measurement uncertainty. The same

color and marker code is used to differentiate which CFD is being compared to. The y-axis uncertainty bars for DCS measurements stem from the width of the laser beam.

5. Uncertainty analysis

The DCS instrument is capable of low uncertainty measurements of multiple flow parameters, as described earlier. However, it is important to consider all potential sources of uncertainty to estimate the total uncertainty of the measurements. We identify the sources of uncertainty to be the DCS instrument accuracy, DCS instrument precision, beam angle, background subtraction, and database. The contribution of each source is described in detail in Supplement 1. Table 1 summarizes the uncertainties stemming from each of these sources for each of the parameters.

The DCS instrument accuracy corresponds to uncertainty stemming from the DCS instrument itself (accuracy and stability of the frequency point spacing and the bandwidth of the system as discussed in Section 2). The DCS instrument precision is the scatter in results due to the noise in the spectrum at 60s of averaging time. We find the scatter by calculating the Allan deviation as shown for velocity in Figure 7. Beam angle uncertainty directly affects velocity as it is essential to relating the Doppler shift to velocity. It also introduces a small difference for other parameters due to a slight uncertainty in the laser pathlength through the flow. Uncertainties due to background subtraction arise from differences in background absorption measured before and after the study measurements. The absorption database adds uncertainty due to error in the absorption model parameters (linestrength, pressure broadening and shift) that form the absorption models used to interpret the measured spectra. Finally, air mass flux uncertainty is calculated by combining the uncertainties for the individual parameters according to Eq. 2.

Table 1. Uncertainty of DCS measurements in run 2

Source/Parameter	Velocity	Pressure	Temperature	χ_{H_2O}	Air Mass Flux
DCS Instrument Accuracy	0.00015%	0.012%	0.015%	0.0042%	0.02%
DCS Instrument Precision	0.17%	0.24%	0.33%	0.73%	0.44%
Beam Angle	0.60%	0.06%	0.01%	0.04%	0.60%
Background Subtraction	0.67%	0.29%	1.1%	0.87%	1.4%
Database Error	0.0%	6.6%	1.2%	9.5%	6.8%
Total	0.91%	6.6%	1.7%	9.6%	6.9%

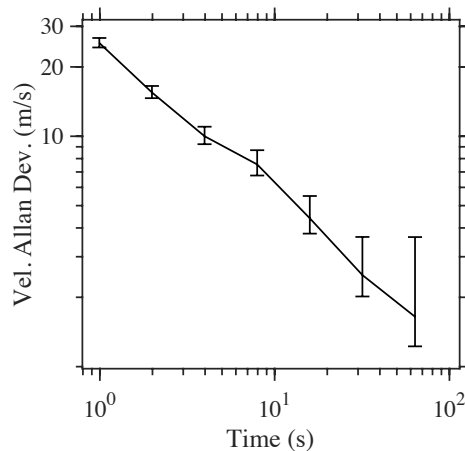


Fig. 7. Allan deviation for velocity from 1s to 60s. Allan deviations for temperature, pressure, and $\chi_{\text{H}_2\text{O}}$ are included in Supplement 1.

Non-DCS sources, especially the absorption database, contribute most of the total uncertainty. We can reasonably expect that uncertainty from non-DCS sources can be improved with better angle determination methods, more vigorous background water vapor purging methods, and database improvement. Thus, overall uncertainty in DCS mass flux measurements can be improved for future measurements.

Uncertainty directly from the DCS instrument (the DCS instrument accuracy and precision) is only $\sim 0.4\%$ at 60s of averaging across all measurements. As the primary uncertainty contribution is from precision, this can be improved with longer averaging times, as the Allan deviation shown in Figure 7 is still declining at 60 seconds. Notably, the velocity precision is < 2 m/s at 60 second averaging. Even at a shorter averaging time of 1 second, we achieve a precision of $\sim 4\%$ (25 m/s), indicating the potential for precise, time-resolved measurements.

6. Discussion

Despite their importance to many atmospheric and industrial applications, direct measurements of mass flux are extremely challenging in large-scale open environments and environments with extreme flow phenomena because it is difficult to simultaneously and non-intrusively measure all of the components of mass flux (i.e. velocity, temperature, pressure, and mixture composition). Here, we demonstrate non-intrusive, absolute measurements of mass flux in such environments by leveraging the unique properties of stabilized, mode-locked frequency combs. In particular, we demonstrate the measurement technique in a supersonic flow environment where the non-intrusive nature of the sensor survives the high temperatures and flow velocities, and the spatial resolution can help with the presence of variable pressure, shock waves, and boundary layers.

Tunable diode lasers have been used for a variety of prior measurements in aerospace environments. Researchers have measured velocity, temperature, or other individual components of mass flux in shock tubes, wind tunnels, and ramjet test models [49–58]. Lyle *et al.* [59] measured mass flow in a cold, subsonic turbofan aeroengine inlet using O_2 -absorption TDLAS. Assuming O_2 mole fraction is fixed, the density of the air at cold temperatures is determined from absorption feature absorbance area using a room temperature calibration. Chang *et al.* [47] and Brown *et al.* [61] made mass flux measurements in supersonic flows. These studies relied on pressure data from wall pressure transducers. Brown *et al.* [48] also measured the pressure with the laser sensor and found a 32% deviation in mass flux values when incorporating direct pressure measurements instead of the facility-measured pressure

value. Thus to the best of our knowledge this is the first study to measure all of the components of mass flux in a supersonic environment with well characterized and low uncertainty.

The ability to localize the pressure, temperature, concentration, velocity, and mass flux to the spatial extent of the laser beam is promising for environments with spatially varying conditions, such as among the boundary layers and pressure shocks that occur in and around hypersonic vehicles. The vertical scan results presented in this paper demonstrate the capability of DCS to measure the spatial variation in the mass flux near the wall of the scramjet isolator. Future measurements could traverse oblique shock trains, incorporating local laser-based pressure measurements rather than potentially non-representative facility wall pressure measurements.

The ability to scan a line-of-sight mass flux measurement through spatially varying conditions can be broadened to other open-area measurements of interest. For example, DCS has been demonstrated for long-distance measurements of trace gases [24,26,28]. The technique shown here could be used to measure spatially resolved or area-averaged mass flux downwind of trace gas sources, such as leaking oil and gas production basins, chemical plants, cities or thawing permafrost without requiring point-based measurements of temperature, pressure or velocity that may misrepresent conditions over the entire beam. More broadly, the large area mass flux approach could have advantages over point-based flux sampling, such as eddy-covariance [62,2,63], for comparisons where representation error is a concern [64–66].

Overall, this demonstration of DCS mass flux sensing with low uncertainty across a difficult suite of flow conditions suggest that DCS is an accurate and multi-faceted sensor with applications across many different environments.

5. Funding and Acknowledgements

This research was sponsored by the Defense Advanced Research Projects Agency (W31P4Q-15-1-0011), the Air Force Office of Scientific Research (FA9550-17-1-0224, FA9550-20-1-0328), and the Air Force Research Laboratories (FA8650-20-2-2418). We thank Amanda Makowiecki for advice performing spectroscopic fits using cepstral analysis and Robbie Wright for building the DCS system and for troubleshooting advice during the campaign. We thank Steve Enneking, Andrew Baron, Justin Stewart, and the facility operators who worked hard to ensure a smooth experimental campaign in Research Cell 18.

References

1. K. L. Mays, P. B. Shepson, B. H. Stirm, A. Karion, C. Sweeney, and K. R. Gurney, "Aircraft-Based Measurements of the Carbon Footprint of Indianapolis," *Environ. Sci. Technol.* **43**, 7816–7823 (2009).
2. E. Velasco and M. Roth, "Cities as Net Sources of CO₂: Review of Atmospheric CO₂ Exchange in Urban Environments Measured by Eddy Covariance Technique," *Geogr. Compass* **4**, 1238–1259 (2010).
3. T. Karl, M. Graus, M. Striednig, C. Lamprecht, A. Hammerle, G. Wohlfahrt, A. Held, L. von der Heyden, M. J. Deventer, A. Krismer, C. Haun, R. Feichter, and J. Lee, "Urban eddy covariance measurements reveal significant missing NO_x emissions in Central Europe," *Sci. Rep.* **7**, 2536 (2017).
4. H. Soegaard and C. Nordstroem, "Carbon dioxide exchange in a high-arctic fen estimated by eddy covariance measurements and modelling," *Glob. Chang. Biol.* **5**, 547–562 (1999).
5. W. C. Oechel, G. L. Vourlitis, S. J. Hastings, R. C. Zulueta, L. Hinzman, and D. Kane, "Acclimation of ecosystem CO₂ exchange in the Alaskan Arctic in response to decadal climate warming," *Nature* **406**, 978–981 (2000).
6. C. Wille, L. Kutzbach, T. Sachs, D. Wagner, and E.-M. Pfeiffer, "Methane emission from Siberian arctic polygonal tundra: eddy covariance measurements and modeling," *Glob. Chang. Biol.* **14**, 1395–1408 (2008).
7. T. F. Keenan, D. Y. Hollinger, G. Bohrer, D. Dragoni, J. W. Munger, H. P. Schmid, and A. D. Richardson, "Increase in forest water-use efficiency as atmospheric carbon dioxide concentrations rise," *Nature* **499**, 324–327 (2013).
8. S. Li, S. Kang, F. Li, and L. Zhang, "Evapotranspiration and crop coefficient of spring maize with plastic mulch using eddy covariance in northwest China," *Agric. Water Manag.* **95**, 1214–1222 (2008).
9. S. S. Anapalli, D. K. Fisher, K. N. Reddy, P. Wagle, P. H. Gowda, and R. Sui, "Quantifying soybean evapotranspiration using an eddy covariance approach," *Agric. Water Manag.* **209**, 228–239 (2018).
10. C. B. Clements, B. E. Potter, S. Zhong, C. B. Clements, B. E. Potter, and S. Zhong, "In situ measurements of water vapor, heat, and CO₂ fluxes within a prescribed grass fire," *Int. J. Wildland Fire* **15**, 299–306 (2006).
11. Q. Sun, W. S. Meyer, G. R. Koerber, and P. Marschner, "Rapid recovery of net ecosystem production in a semi-arid woodland after a wildfire," *Agric. For. Meteorol.* **291**, 108099 (2020).
12. J. Teng and H. Yuan, "Variable geometry cowl sidewall for improving rectangular hypersonic inlet performance," *Aerosp. Sci. Technol.* **42**, 128–135 (2015).
13. C. Park, G. A. Raiche, D. M. Driver, J. Olejniczak, I. Terrazas-Salinas, T. M. Hightower, and T. Sakai, "Comparison of Enthalpy Determination Methods for an Arc-Jet Facility," *J. Thermophys. Heat Transf.* **20**, 672–679 (2006).
14. M. L. Fotia, J. Hoke, and F. Schauer, "Experimental Performance Scaling of Rotating Detonation Engines Operated on Gaseous Fuels," *J. Propuls. Power* **33**, 1187–1196 (2017).
15. J. Hank, J. Murphy, and R. Mutzman, "The X-51A Scramjet Engine Flight Demonstration Program," in *15th AIAA International Space Planes and Hypersonic Systems and Technologies Conference* (American Institute of Aeronautics and Astronautics, n.d.).
16. K. R. Jackson, M. R. Gruber, and S. Buccellato, "Mach 6–8+ Hydrocarbon-Fueled Scramjet Flight Experiment: The HIFiRE Flight 2 Project," *J. Propuls. Power* **31**, 36–53 (2015).
17. M. Yu, Y. Okawachi, A. G. Griffith, N. Picqué, M. Lipson, and A. L. Gaeta, "Silicon-chip-based mid-infrared dual-comb spectroscopy," *Nat. Commun.* **9**, 1869 (2018).

18. K. Krzempek, D. Tomaszewska, A. Głuszek, T. Martynkien, P. Mergo, J. Sotor, A. Foltynowicz, and G. Soboń, "Stabilized all-fiber source for generation of tunable broadband fCEO-free mid-IR frequency comb in the 7 – 9 μm range," *Opt. Express* **27**, 37435 (2019).
19. M. A. Abbas, A. Khodabakhsh, Q. Pan, J. Mandon, S. M. Cristescu, and F. J. M. Harren, "Mid-infrared dual-comb spectroscopy with absolute frequency calibration using a passive optical reference," *Opt. Express* **27**, 19282–19291 (2019).
20. G. Ycas, G. Ycas, F. R. Giorgetta, F. R. Giorgetta, J. T. Friedlein, D. Herman, D. Herman, K. C. Cossel, E. Baumann, E. Baumann, N. R. Newbury, and I. Coddington, "Compact mid-infrared dual-comb spectrometer for outdoor spectroscopy," *Opt. Express* **28**, 14740–14752 (2020).
21. A. Makowiecki, D. I. Herman, N. Hoghooghi, E. F. Strong, R. K. Cole, G. G. Ycas, F. R. Giorgetta, C. B. Lapointe, J. F. Glusman, J. W. Daily, P. E. Hamlington, N. R. Newbury, I. R. Coddington, and G. B. Rieker, "Mid-Infrared Dual Frequency Comb Spectroscopy for Combustion Analysis from 2.8 to 5 Microns," *Proc. Combust. Inst.* **38**, (2020).
22. N. H. Pinkowski, Y. Ding, C. L. Strand, R. K. Hanson, R. Horvath, and M. Geiser, "Dual-comb spectroscopy for high-temperature reaction kinetics," *Meas. Sci. Technol.* **31**, 055501 (2020).
23. D. M. B. Lesko, H. Timmers, S. Xing, A. Kowligy, A. J. Lind, and S. A. Diddams, "A six-octave optical frequency comb from a scalable few-cycle erbium fibre laser," *Nat. Photonics* **15**, 281–286 (2021).
24. G. B. Rieker, F. R. Giorgetta, W. C. Swann, J. Kofler, A. M. Zolot, L. C. Sinclair, E. Baumann, C. Cromer, G. Petron, C. Sweeney, P. P. Tans, I. Coddington, and N. R. Newbury, "Frequency-comb-based remote sensing of greenhouse gases over kilometer air paths," *Optica* **1**, 290–298 (2014).
25. S. Coburn, C. B. Alden, R. Wright, K. Cossel, E. Baumann, G.-W. Truong, F. Giorgetta, C. Sweeney, N. R. Newbury, K. Prasad, I. Coddington, and G. B. Rieker, "Regional trace-gas source attribution using a field-deployed dual frequency comb spectrometer," *Optica* **5**, 320–327 (2018).
26. E. M. Waxman, K. C. Cossel, F. Giorgetta, G.-W. Truong, W. C. Swann, I. Coddington, and N. R. Newbury, "Estimating vehicle carbon dioxide emissions from Boulder, Colorado, using horizontal path-integrated column measurements," *Atmos. Chem. Phys.* **19**, 4177–4192 (2019).
27. J. Liu, C. C. Teng, Y. Chen, C. L. Patrick, J. Westberg, J. Westberg, and G. Wysocki, "Field deployment of a multi-pass cell based mid-IR quantum cascade laser dual-comb spectrometer," in *Conference on Lasers and Electro-Optics (2021), Paper AW2S.1* (Optical Society of America, 2021), p. AW2S.1.
28. D. I. Herman, C. Weerasekara, L. C. Hutcherson, F. R. Giorgetta, K. C. Cossel, E. M. Waxman, G. M. Colacion, N. R. Newbury, S. M. Welch, B. D. DePaola, I. Coddington, E. A. Santos, and B. R. Washburn, "Precise multispecies agricultural gas flux determined using broadband open-path dual-comb spectroscopy," *Sci. Adv.* (2021).
29. A. G. Griffith, R. K. W. Lau, J. Cardenas, Y. Okawachi, A. Mohanty, R. Fain, Y. H. D. Lee, M. Yu, C. T. Phare, C. B. Poitras, A. L. Gaeta, and M. Lipson, "Silicon-chip mid-infrared frequency comb generation," *Nat. Commun.* **6**, 6299 (2015).
30. Myoung-Gyun Suh, Qi-Fan Yang, Ki Youl Yang, Xu Yi, and Kerry J. Vahala, "Microresonator soliton dual-comb spectroscopy," *Science* **354**, 600–603 (2016).
31. V. Brasch, M. Geiselmann, T. Herr, G. Lihachev, M. H. P. Pfeiffer, M. L. Gorodetsky, and T. J. Kippenberg, "Photonic chip-based optical frequency comb using soliton Cherenkov radiation," *Science* **351**, 357–360 (2016).
32. M. Yan, P.-L. Luo, K. Iwakuni, G. Millot, T. W. Hänsch, and N. Picqué, "Mid-infrared dual-comb spectroscopy with electro-optic modulators," *Light. Sci. Appl.* **6**, e17076–e17076 (2017).

33. P. Guay, J. Genest, and A. J. Fleisher, "Precision spectroscopy of H^{13}CN using a free-running, all-fiber dual electro-optic frequency comb system," *Opt. Lett.* **43**, 1407–1410 (2018).
34. D. A. Long, D. A. Long, B. J. Reschovsky, F. Zhou, Y. Bao, T. W. LeBrun, J. J. Gorman, and J. J. Gorman, "Electro-optic frequency combs for rapid interrogation in cavity optomechanics," *Opt. Lett.* **46**, 645–648 (2021).
35. L. C. Philippe and R. K. Hanson, "Laser-absorption mass flux sensor for high-speed airflows," *Opt. Lett.* **16**, 2002–2004 (1991).
36. N. R. Newbury, "Searching for applications with a fine-tooth comb," *Nat. Photonics* **5**, 186–188 (2011).
37. N. Picqué and T. W. Hänsch, "Frequency comb spectroscopy," *Nat. Photonics* **13**, 146–157 (2019).
38. I. Coddington, N. Newbury, and W. Swann, "Dual-comb spectroscopy," *Optica* **3**, 414–426 (2016).
39. L. C. Sinclair, I. Coddington, W. C. Swann, G. B. Rieker, A. Hati, K. Iwakuni, and N. R. Newbury, "Operation of an optically coherent frequency comb outside the metrology lab," *Opt. Express* **22**, 6996 (2014).
40. H. R. Telle, G. Steinmeyer, A. E. Dunlop, J. Stenger, D. H. Sutter, and U. Keller, "Carrier-envelope offset phase control: A novel concept for absolute optical frequency measurement and ultrashort pulse generation," *Appl. Phys. B* **69**, 327–332 (1999).
41. J. Reichert, R. Holzwarth, Th. Udem, and T. W. Hänsch, "Measuring the frequency of light with mode-locked lasers," *Optics Communications* **172**, 59–68 (1999).
42. G.-W. Truong, E. M. Waxman, K. C. Cossel, E. Baumann, A. Klose, F. R. Giorgetta, W. C. Swann, N. R. Newbury, and I. Coddington, "Accurate frequency referencing for fieldable dual-comb spectroscopy," *Opt. Express*, OE **24**, 30495–30504 (2016).
43. E. M. Waxman, K. C. Cossel, G.-W. Truong, F. R. Giorgetta, W. C. Swann, S. Coburn, R. J. Wright, G. B. Rieker, I. Coddington, and N. R. Newbury, "Intercomparison of Open-Path Trace Gas Measurements with Two Dual Frequency Comb Spectrometers," *Atmos. Meas. Tech.* **10**, 3295–3311 (2017).
44. R. K. Cole, A. S. Makowiecki, N. Hoghooghi, and G. B. Rieker, "Baseline-free Quantitative Absorption Spectroscopy Based on Cepstral Analysis," *Opt. Express* **27**, (2019).
45. A. D. Draper, R. K. Cole, A. S. Makowiecki, J. Mohr, A. Zdanowicz, A. Marchese, N. Hoghooghi, and G. B. Rieker, "Broadband dual-frequency comb spectroscopy in a rapid compression machine," *Opt. Express* **27**, 10814–10825 (2019).
46. K.-C. Lin, K. Jackson, R. Behdadnia, T. A. Jackson, F. Ma, and V. Yang, "Acoustic Characterization of an Ethylene-Fueled Scramjet Combustor with a Cavity Flameholder," *J. Propuls. Power* **26**, 1161–1170 (2010).
47. P. J. Schroeder, D. J. Pfothauer, J. Yang, F. R. Giorgetta, W. C. Swann, I. Coddington, N. R. Newbury, and G. B. Rieker, "High temperature comparison of the HITRAN2012 and HITEMP2010 water vapor absorption databases to frequency comb measurements," *J. Quant. Spectrosc. Radiat. Transf.* **203**, 194–205 (2017).
48. L. S. Rothman, I. E. Gordon, Y. Babikov, A. Barbe, D. Chris Benner, P. F. Bernath, M. Birk, L. Bizzocchi, V. Boudon, L. R. Brown, A. Campargue, K. Chance, E. A. Cohen, L. H. Coudert, V. M. Devi, B. J. Drouin, A. Fayt, J.-M. Flaud, R. R. Gamache, J. J. Harrison, J.-M. Hartmann, C. Hill, J. T. Hodges, D. Jacquemart, A. Jolly, J. Lamouroux, R. J. Le Roy, G. Li, D. A. Long, O. M. Lyulin, C. J. Mackie, S. T. Massie, S. Mikhailenko, H. S. P. Müller, O. V. Naumenko, A. V. Nikitin, J. Orphal, V. Perevalov, A. Perrin, E. R. Polovtseva, C. Richard, M. A. H. Smith, E. Starikova, K. Sung, S. Tashkun, J. Tennyson, G. C. Toon, Vl. G. Tyuterev, and G. Wagner, "The HITRAN2012 molecular spectroscopic database," *J. Quant. Spectrosc. Radiat. Transf.* **130**, 4–50 (2013).

49. G. B. Rieker, J. B. Jeffries, and R. K. Hanson, "Calibration-free wavelength-modulation spectroscopy for measurements of gas temperature and concentration in harsh environments," *Appl. Opt.* **48**, 5546–5560 (2009).
50. L. C. Philippe and R. K. Hanson, "Laser diode wavelength-modulation spectroscopy for simultaneous measurement of temperature, pressure, and velocity in shock-heated oxygen flows," *Appl. Opt.* **32**, 6090–6103 (1993).
51. B. L. Upschulte, M. F. Miller, and M. G. Allen, "Diode Laser Sensor for Gasdynamic Measurements in a Model Scramjet Combustor," *AIAA Journal* **38**, 1246–1252 (2000).
52. J. T. C. Liu, G. B. Rieker, J. B. Jeffries, M. R. Gruber, C. D. Carter, T. Mathur, and R. K. Hanson, "Near-infrared diode laser absorption diagnostic for temperature and water vapor in a scramjet combustor," *Appl. Opt.* **44**, 6701–6711 (2005).
53. F. Li, X. Yu, H. Gu, Z. Li, Y. Zhao, L. Ma, L. Chen, and X. Chang, "Simultaneous measurements of multiple flow parameters for scramjet characterization using tunable diode-laser sensors," *Appl. Opt.* **50**, 6697–6707 (2011).
54. G. B. Rieker, J. B. Jeffries, R. K. Hanson, T. Mathur, M. R. Gruber, and C. D. Carter, "Diode laser-based detection of combustor instabilities with application to a scramjet engine," *Proc. Combust. Inst.* **32**, 831–838 (2009).
55. C. L. Strand and R. K. Hanson, "Quantification of Supersonic Impulse Flow Conditions via High-Bandwidth Wavelength Modulation Absorption Spectroscopy," *AIAA Journal* **53**, 2978–2987 (2015).
56. K. M. Busa, B. E. Rice, J. C. McDaniel, C. P. Goyne, R. D. Rockwell, J. A. Fulton, J. R. Edwards, and G. S. Diskin, "Scramjet Combustion Efficiency Measurement via Tomographic Absorption Spectroscopy and Particle Image Velocimetry," *AIAA Journal* **54**, 2463–2471 (2016).
57. Z. Xu, R. Kan, J. Ran, L. Yao, X. Fan, and J. Liu, "A Tunable Diode Laser Absorption Based Velocity Sensor for Local Field in Hypersonic Flows," in *Light, Energy and the Environment (2016), Paper ETu2A.4* (Optica Publishing Group, 2016), p. ETu2A.4.
58. J. Kurtz, M. Aizengendler, Y. Krishna, P. Walsh, and S. O'Byrne, "Rugged, Scramjet Inlet Temperature and Velocity Sensor: Design and Ground Test," *AIAA Journal* **54**, 399–407 (2016).
59. K. H. Lyle, J. B. Jeffries, R. K. Hanson, and M. Winter, "Diode-Laser Sensor for Air-Mass Flux 2: Non-Uniform Flow Modeling and Aeroengine Tests," *AIAA Journal* **45**, 2213–2223 (2007).
60. L. S. Chang, C. L. Strand, J. B. Jeffries, R. K. Hanson, G. S. Diskin, R. L. Gaffney, and D. P. Capriotti, "Supersonic Mass-Flux Measurements via Tunable Diode Laser Absorption and Nonuniform Flow Modeling," *AIAA Journal* **49**, 2783–2791 (2011).
61. M. Brown, D. Barone, T. Barhorst, D. Eklund, M. Gruber, T. Mathur, and R. Milligan, "TDLAS-based Measurements of Temperature, Pressure, and Velocity in the Isolator of an Axisymmetric Scramjet," in *46th AIAA/ASME/SAE/ASEE Joint Propulsion Conference & Exhibit* (American Institute of Aeronautics and Astronautics, 2010).
62. D. D. Baldocchi, "Assessing the eddy covariance technique for evaluating carbon dioxide exchange rates of ecosystems: past, present and future," *Glob. Chang. Biol.* **9**, 479–492 (2003).
63. M. Aubinet, T. Vesala, and D. Papale, *Eddy Covariance: A Practical Guide to Measurement and Data Analysis* (Springer Science & Business Media, 2012).
64. R. Oren, C.-I. Hsieh, P. Stoy, J. Albertson, H. R. McCarthy, P. Harrell, and G. G. Katul, "Estimating the uncertainty in annual net ecosystem carbon exchange: spatial variation in turbulent fluxes and sampling errors in eddy-covariance measurements," *Glob. Chang. Biol.* **12**, 883–896 (2006).
65. T. Hill, M. Chocholek, and R. Clement, "The case for increasing the statistical power of eddy covariance ecosystem studies: why, where and how?," *Glob. Chang. Biol.* **23**, 2154–2165 (2017).

66. M. M. T. A. Pallandt, J. Kumar, M. Mauritz, E. A. G. Schuur, A.-M. Virkkala, G. Celis, F. M. Hoffman, and M. Göckede, "Representativeness assessment of the pan-Arctic eddy covariance site network and optimized future enhancements," *Biogeosciences* **19**, 559–583 (2022).

Spatially resolved mass flux measurements with dual comb spectroscopy: supplemental document

1. Velocimetry with crossed laser beams

Doppler shift refers to the phenomenon where the bulk velocity, U , of the absorbing molecules moving toward or away from the laser propagation direction shifts the expected frequency position of absorption features, ν_0 , to a new position, ν , according to Eq. S1:

$$\nu = \left(1 + \frac{U \sin \theta}{c}\right) \nu_0 \quad (S1)$$

θ is the angle between the laser line-of-sight and the normal to the flow direction and c is the speed of sound. Eq. S1 describes an ideal situation where there is no absolute frequency error (not to be confused with drift in the spacing of the comb teeth) or absorption model error. If these effects are included, the Doppler shift is described by:

$$\nu = \left(1 + \frac{U \sin \theta}{c}\right) (\nu_0 + \delta_{ab}) + \delta_s \quad (S2)$$

Where δ_s is the absolute frequency error of the spectrometer and δ_{ab} is the absorption model error ('database' error). Absorption model error can be induced by incorrect line center position, pressure shift, and temperature dependence of pressure shift parameters for absorption features in the model. However, if we take the difference between a laser path angled upstream and a laser path angled downstream at the same angle, $\nu_u - \nu_d$, the frequency shift due to the spectrometer, δ_s , cancels as it is the same for both paths. Furthermore, if we assume that both laser paths sample the flow across equal thermodynamic conditions (such that δ_{ab} is the same for both paths), that δ_{ab} is small compared to the absorption position at static conditions, ν_0 , and that the angles are equal and opposite, we see from the following expression that database error and wavenumber drift do not affect the velocity fit from the dual-beam setup:

$$U = \frac{c(\nu_u - \nu_d)}{2\nu_0 \sin \theta} \quad (S3)$$

It should be noted that though spectrometer absolute frequency error and drift can be overcome using the crossed-beam approach, errors in relative measurements of frequencies due to changes or uncertainties in the spectrometer point spacing (comb tooth spacing) cannot. Accuracy of the point spacing directly affects measurement of $\nu_u - \nu_d$ in the same way that a correct measurement of distance between two points on a ruler depends on the accuracy of its tick spacing. In DCS, the spectral point spacing is determined by the pulse rate, which is measured throughout comb operation with a counter that is clocked by the oven-controlled quartz oscillator (OCXO) mentioned in Section 2. This oscillator, when accounting for stated product typical aging behavior, is expected to demonstrate a relative accuracy of 1.5×10^{-6} . Consequently, this leads to a 1.5×10^{-6} uncertainty in the DCS pulse rate and spectral point spacing which directly translates to velocity uncertainty of the same magnitude -1.5×10^{-6} or 0.00015%. To put this in perspective, the pulse rate control in the DCS can be compared to the etalon used in tunable diode laser absorption spectroscopy to continuously measure the tuning rate of the laser. To achieve the same sort of relative wavenumber error as the DCS system used here, the TDLAS etalon length would need to be known and maintained within 0.00015%.

Additionally, as point spacing also determines measurement of linewidths, the point spacing uncertainty contribution to pressure measurements is also just 0.00015%.

2. Fitting DCS spectra

DCS (and laser absorption spectroscopy in general) measures laser absorption at frequencies resonant with the rovibrational quantum state transitions of a constituent molecule in a gas sample or flow. Pressure, species concentration, velocity, and temperature of the probed region of the flow can be determined by comparing the size, shape, and position of measured absorption features with an absorption model of the expected spectra for a given set of conditions. Figure S1 shows a small portion of the spectra of Run 1 and Run 5 to demonstrate the large differences in the measured spectra that are generated by the different velocity, pressure, temperature, and species concentrations of the two runs. The run conditions are determined by fitting absorption models to the measured spectra.

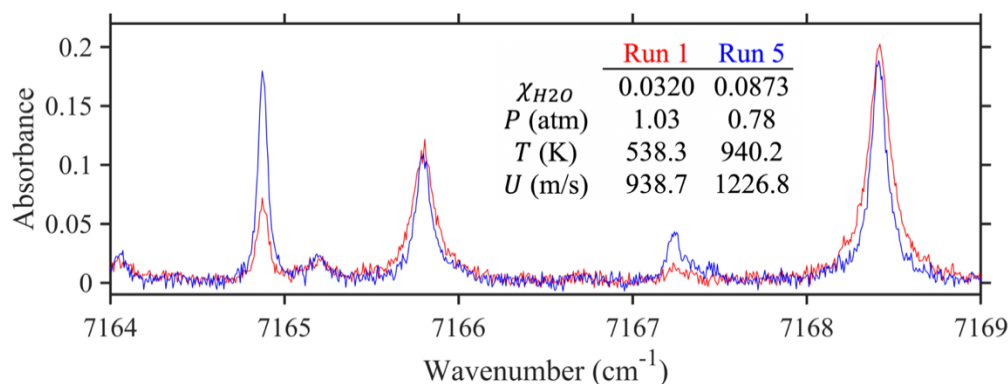


Fig. S1. A zoom-in of upstream spectra from a high-pressure, low-velocity condition (Run 1, red) and a low-pressure, high-velocity condition (Run 5, blue). Run 1 demonstrates wider FWHM of features due to greater P_{tot} . Different temperatures manifest in the differing ratio of heights of the features (see ratio of feature at 7164.9 cm^{-1} to that of 7165.8 cm^{-1}). The Doppler shift due to velocity is not apparent at this scale. Additionally, trends in χ_{H_2O} are also not apparent when comparing spectra of two different pressures and temperatures.

Specifically, spectra from the upstream and downstream paths (see Figure 3 for an example) are fit simultaneously to models derived from Schroeder et al. [1] using the modified free induction decay analysis approach [2]. The fits are constrained to retrieve a single temperature, pressure, velocity, and H_2O concentration across the laser pathlength and between both the upstream and downstream beam. Thus, the absorption models for the upstream and downstream beams for a single measurement are identical besides the equal and opposite Doppler shifts due to the equal and opposite angles of the two paths.

3. Contributions to uncertainty

3.1 DCS instrument uncertainty

The DCS instrument provides a stable frequency axis and broad bandwidth that enable low instrument uncertainty. To determine uncertainty due to the DCS instrument, we fit simulated spectra over the same bandwidth as the measurements with frequency axes that are distorted by 1.5 ppm (the uncertainty of the frequency axis as described in section 2 of the paper). This method couples in the possible interplay of uncertainty in the frequency axis and the absorption model fit to the measurement. Velocity demonstrates a 0.00015% error as a result of frequency axis uncertainty. This directly matches the frequency axis uncertainty, as expected since any error in the frequency axis should directly translate to shift measurement error and thus error in the velocity retrieval. The pressure retrieval demonstrates 0.012% error due to frequency axis

uncertainty. While pressure correlates to feature width, which is directly related to the frequency axis error, complexities in the absorption model and correlation with temperature and concentration uncertainty (since all four parameters are retrieved simultaneously) make the pressure error higher than the 1.5 ppm frequency axis error. The concentration and temperature retrievals demonstrate errors of 0.015% and 0.0042%, respectively, as a result of uncertainty in the frequency axis.

The errors from these simulated fits are taken to be the uncertainty due to DCS instrument accuracy in Table I. Overall, this leads to a 0.02% uncertainty in the DCS mass flux measurements. There are other sources of uncertainty that can contribute to DCS instrument accuracy such as RF detection equipment and optical paths as outlined in Waxman *et al.* [3]. Unfortunately these uncertainties could not be determined for our setup. However, we expect these uncertainties to be negligibly small. Waxman *et al.* [3] found just a 56 ppm instrument accuracy for χ_{H_2O} for a similar DCS system.

3.2 DCS instrument precision

The contribution of the DCS instrument precision to uncertainty is determined from Allan deviation analyses for each parameter. The Allan deviation quantifies the deviation of repeated measurements from the mean value as a function of averaging time. Thus, the Allan deviation assesses statistical uncertainty in the measurements, not systematic uncertainty (which describes all of the other sources we quantify in Supplement 3).

The Allan deviations for each of the measured parameters are show in Figure S2. In general, all of the measured parameters exhibit the $\tau^{-1/2}$ slope associated with white noise. Meaning that as we continue to average spectra together, the precision of the measurements improve, mostly due to improving absorbance noise on the measured spectra. For the measurements we report in Figures 4 and 6, we averaged for 60s. Thus, we estimate the instrument precision from the Allan deviation for that averaging time.

For 60 s averages, the Allan deviation is 1.6 m/s for velocity, 1.7×10^{-3} atm for pressure, 1.8 K for temperature, and 2.8×10^{-4} for χ_{H_2O} . This amounts to a $2.0 \text{ kg/m}^2\text{-s}^{-1}$ deviation for air mass flux. Thus, the precision of the measurements is very good, and can be further improved with more averaging or better signal-to-noise ratio of the DCS measurement. As shown in Table 2 of the main text, the precision contributes sub-percent uncertainties for run 2.

Note that at 1s, the Allan deviations are 25 m/s for velocity, 7.6 K for temperature, 1.5×10^{-3} atm for pressure, 7.9×10^{-4} for χ_{H_2O} , and $16.5 \text{ kgm}^{-2}\text{s}^{-1}$ for air mass flux. When applied to run 2, this amounts to 2.66%, 1.41%, 2.08%, 2.05%, and 3.67% for the same parameters respectively, indicating the potential for time-resolved DCS measurements even in the current configuration.

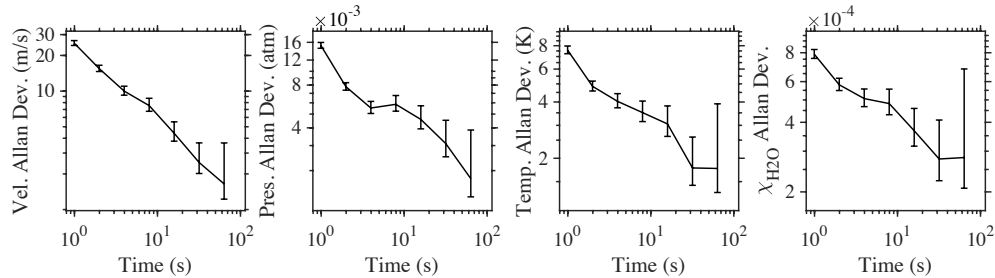


Fig. S2. Allan deviations for velocity, pressure, temperature, and χ_{H_2O}

3.3 Beam angle

We set the beam angle for the experimental setup with high precision rotation mounts. While these rotation mounts allow for 5 arcsecond precision, the uncertainty in our beam angle

was determined by human ability to accurately position the mounts. We determined that this was limited to being able to set the angle within 0.25° . As per Eq. 6, this introduces a relative uncertainty in the velocity of 0.6%. In order to determine how beam angle might affect the other flow values, we simulated upstream and downstream spectra and fit with a 0.25° error in the angle. Temperature, pressure, and χ_{H_2O} were found to deviate from the true (simulated) values by only 0.011%, 0.061%, and 0.38% respectively. Additionally, this simulated fit confirmed the expected 0.6% velocity error.

3.4 Background subtraction

As shown in Figure 1, a portion of the laser beam path passes through an open path between the collimating optics and the window of the test section. There is also an open path in the free-space optical filters. In total, these paths result in ~ 115 cm of open beam path that is not inside the test section for each laser. Because room air contains H_2O , there is potential for water vapor absorption outside the isolator, which we refer to as background absorption. In order to minimize background absorption, the free-space filter and the open paths near the transmit and receive optics were all purged with dry air. However, even with the purge system some small amount of background H_2O remains along the path. To determine this amount, pre- and post-background spectral measurements are taken with a well-defined vacuum flow in the test engine before and after the testing session. Once the background absorption is determined, a background model is created and then subtracted from the data to remove the effect of background absorption on the final results.

We found that the background absorption slightly differs in the pre-measurement and post-measurement background scans that we took. These differences can lead to different retrieve parameters in the measurement based on which background model was subtracted from the data. Figure S3 demonstrates these differences for velocity in the centerline runs. Averages between the two fits resulting from pre- and post-background subtraction are presented as the fit results in Section 4. The difference between the average reported result and the original background subtraction results leads to a 0.8-1.4% mass flux uncertainty across the tests runs.

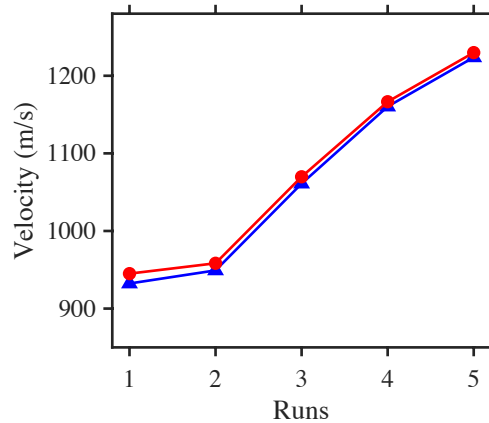


Fig. S3. DCS fitted velocities for centerline runs after treatment with pre-background (red) and post-background (blue). A slight difference between the two is seen.

3.5 Database

The spectroscopic database which is used to create the absorption model contributes the most uncertainty to the mass flux measurements. As mentioned before, the DCS broad bandwidth is advantageous for reducing scatter in model errors among individual absorption features. However, general biases across the whole bandwidth will be reflected in the DCS measurements. Velocity is the exception as it is unaffected by database error due to the dual-

beam setup, as discussed in Supplement 1. We determined database uncertainty by fitting experimental data sets at known conditions of 500 to 900 K and 0.4 to 0.8 atm with the database used here, Schroeder et al. [1]. The largest deviations were reported as the uncertainties for pressure, temperature, and χ_{H_2O} . χ_{H_2O} was found to have the largest uncertainty of the three at 9.5%, while pressure and χ_{H_2O} had 6.6% and 9.5% database uncertainty. Ref. [1] improves on pure H₂O absorption model parameters (e.g. position, self shift, self broadening, linestrength) in HITRAN2012 but does not include improvements to model parameters most relevant to pressure measurements in a H₂O-air mixture (e.g. air broadening and shift). It should be noted that since pressure and χ_{H_2O} are somewhat correlated in the absorption model, some of the database uncertainty for χ_{H_2O} might be explained as the fitting algorithm compensating for pressure errors. Thus, these results indicate that much of the mass flux uncertainty can be improved with a database study focused on H₂O-air pressure broadening and shift parameters for high temperature environments.

4. RC-18 test facility

Research Cell 18 at Wright Patterson Air Force Base houses a ground-test dual-mode ramjet engine (Figure S4). To simulate in-flight flows, the test section consists of isolator, combustor, and expansion nozzle sections similar to flight engines, but with the addition of a preceding combustor heater (or vitiator, not shown in Figure S4) and a converging-diverging nozzle. The vitiator and pre-nozzle condition the incoming air to simulate the high-speed air entering the isolator during flight. In order to compensate for oxygen lost in the pre-combustion, make-up oxygen can be added to the flow. As shown in Table SI, only run 2 had full make-up oxygen as the oxygen supply was low and was not required for these particular tests.

Typically, in-flight isolators compress air through a series of oblique shocks which can be replicated in the RC-18 isolator via a distortion generator. However, this component was not included for this study to maintain well known conditions for comparison with the measurements. Static pressure sensors line the top and bottom of the test isolator in 1.3 cm intervals. An interpolation of these readings is used to provide the pressure conditions in Table SI.

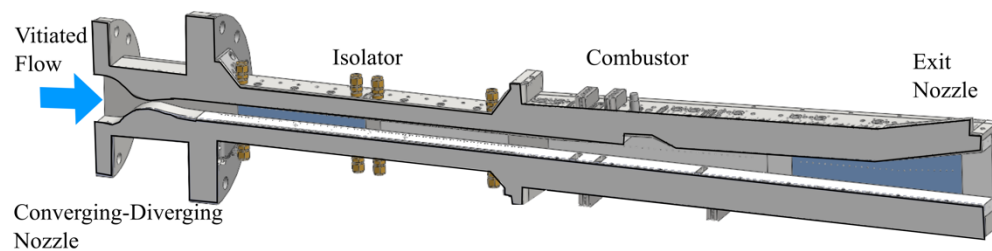


Fig. S4. Cross-section of RC-18 dual mode ramjet test engine. The engine receives flow that is vitiated by a preceding combustor. The converging-diverging nozzle accelerates the air to flight conditions. The isolator compresses and decelerates the air. The combustor heats the flow by injecting fuel and igniting the flow in the flame-holding cavity. The exit nozzle accelerates the air to produce thrust.

6. Measurement Conditions

Table S1. Measurement Conditions

Run	1D Comp. Flow Calculated Velocity (m/s) ¹	1D Comp. Flow Calculated Temperature (K) ¹	Pressure (atm) ²	Measurement Height (mm) ³	Make-up O ₂ Level ⁴
1	942	528	1.08	19	Reduced
2	964	529	0.79	19	Full
3	1066	678	0.81	19	Reduced
4	1160	838	0.83	19	Reduced
5	1215	918	0.83	19	Reduced
6	963	529	0.83	9	Reduced
7	963	529	0.84	3	Reduced
8	963	529	0.84	2	Reduced
9	963	529	0.85	1	Reduced

¹1D variable-gamma compressible flow calculations

²Interpolated to measurement area from top and bottom wall pressure transducer readings

³From bottom of isolator

⁴Make-up O₂ is discussed in Section 4

References

1. P. J. Schroeder, M. J. Cich, J. Yang, F. R. Giorgetta, W. C. Swann, I. Coddington, N. R. Newbury, B. J. Drouin, and G. B. Rieker, "Speed-dependent Voigt lineshape parameter database from dual frequency comb measurements up to 1305 K. Part I: Pure H₂O absorption, 6801–7188 cm⁻¹," *J. Quant. Spectrosc. Radiat. Transfer* **210**, 240–250 (2018).
2. A. Makowiecki R. Cole, N. Hoghooghi and G. Rieker, "Baseline Free Absorption Spectroscopy," in (2019).
3. E. M. Waxman, K. C. Cossel, G.-W. Truong, F. R. Giorgetta, W. C. Swann, S. Coburn, R. J. Wright, G. B. Rieker, I. Coddington, and N. R. Newbury, "Intercomparison of Open-Path Trace Gas Measurements with Two Dual Frequency Comb Spectrometers," *Atmos Meas Tech* **10**, 3295–3311 (2017).